Final Draft

of the original manuscript

Li, J.; Fang, F.; Steppeler, J.; Zhu, J.; Cheng, Y.; Wu, X.:

Demonstration of a three-dimensional dynamically adaptive atmospheric dynamic framework for the simulation of mountain waves.

In: Meteorology and Atmospheric Physics. Vol. 133 (2021) 6, 1627 - 1645.

First published online by Springer: 21.09.2021

https://dx.doi.org/10.1007/s00703-021-00828-8

Demonstration of a Three-Dimensional Dynamically Adaptive Atmospheric Dynamic Framework for the Simulation of Mountain Waves

J. Li[1,2*], F. Fang[3], J. Steppeler[4], J. Zhu[1,5], Y. Cheng[6], X. Wu[3]

[1]International Center for Climate and Environment Sciences, Institute of Atmospheric Physics, Chinese Academy of Sciences, Beijing, 100029, China

[2] Department of Applied Mathematics and Theoretical Physics, Centre for Mathematical Sciences, Wilberforce Road CB3 0WA, United Kingdom

[3]Applied Modelling and Computation Group, Department of Earth Science and Engineering, Imperial College London, London SW7 2AZ, United Kingdom

[4] Climate Service Center Germany (GERICS), Hamburg 20095, Germany

[5] Department of Atmospheric Sciences, University of Chinese Academy of Sciences, Beijing 100049, China

[6] Key Laboratory of Atmospheric Sounding, Chengdu University of Information Technology, Chengdu 610225, China

Corresponding author J. Li

Telephone: +86-10-82995206

E-mail: ljx2311@mail.iap.ac.cn

ORCID: 0000-0001-8924-5220

Abstract

In this paper, Fluidity-Atmosphere, representative of a three-dimensional (3D) nonhydrostatic Galerkin compressible atmospheric dynamic framework, is generated to resolve large-scale and small-scale phenomena simultaneously. This achievement is facilitated by the use of nonhydrostatic equations and the adoption of a flexible 3D dynamically adaptive mesh where the mesh is denser in areas with higher gradients of variable solutions and relatively sparser in the rest of the domain while maintaining promising accuracy and reducing computational resource requirements. The dynamic core is formulated based on anisotropic tetrahedral meshes in both the horizontal and vertical directions. The performance of the adaptive mesh techniques in Fluidity-Atmosphere is evaluated by simulating the formation and propagation of a nonhydrostatic mountain wave. The 2D anisotropic adaptive mesh shows that the numerical solution is in good agreement with the analytic solution. The variation in the horizontal and vertical resolutions has a strong impact on the smoothness of the results and maintains convergence even at high resolutions. When the simulation is extended to 3D, Fluidity-Atmosphere shows stable and symmetric results in the benchmark test cases. The flows over a bell-shaped mountain are resolved quite smoothly. For steep mountains, Fluidity-Atmosphere performs very well, which shows the potential of using 3D adaptive meshes in atmospheric modeling. Finally, as an alternative cut-cell mesh in Fluidity-Atmosphere, the anisotropic adaptive mesh coupled with the Galerkin method provides an alternative accurate representation of terrain-induced flow.

Keywords

Fluidity-Atmosphere

Dynamically Adaptive Mesh

Mountain Wave

Galerkin Method

1. Introduction

Atmospheric motion involves a wide range of spatial scales, from large-scale flows O(10^6-10^7) *m* down to parameterized turbulence O(10^1-10^2) *m* (Kühnlein 2011; Zheng et al. 2015). In numerical weather prediction (NWP) models, the straightforward way to resolve more small-scale phenomena is by using a high-resolution mesh, which leads to a high computational cost. However, it is often not feasible to use a global uniform high-resolution mesh to simulate large- and small-scale phenomena simultaneously with limited computational resources. In recent decades, the adoption of adaptive mesh refinement has solved this bottleneck by locally increasing the mesh resolution in the key domain of NWP models and leaving a coarse resolution for the rest of the model. Adaptive mesh refinement can be distinguished into static and dynamic refinement (Marras et al. 2016). For static mesh refinement, resolution adjustment is always achieved by hierarchical mesh nesting, which has been widely used in many NWP models: WRF (Skamarock et al. 2007), GRAPES (Yang et al. 2008), COSMO (Steppeler et al. 2002; Doms and Baldauf 2018), NAM (Janjic 2003), RAMS (Pielke et al. 1992), etc. For dynamic mesh refinement, the mesh is adjusted in time and space, thereby enabling multiscale processes to be resolved and the features of flows to be captured as time evolves. Skamarock et al. (1989) and Skamarock and Klemp (1993) first applied adaptive meshes in atmospheric sciences. Bacon et al. (1999) developed the first operational adaptive model, the operational multiscale environment model with grid adaptivity (OMEGA), and simulated hurricane tracks with a horizontal adaptive mesh. Iselin (2002) utilized a stretched adaptive mesh to address 1D and 2D advection problems. St-Cyr et al. (2008) compared two shallow-water models with quad-tree adaptive mesh refinement and demonstrated that the adaptive mesh was able to track features of interest without visible distortion at the mesh interfaces. Weller et al. (2016) introduced a new *r*-adaptive mesh using optimal transport and the numerical solution of a Monge-Ampère type equation. Furthermore, the adaptive mesh has been a strong competitor in resolving multiscale dynamic and chemical processes (Garcia-Menendez and Odman 2011; Karamchandani et al. 2011). Odman and Khan (2002) and Odman et al. (2004) introduced adaptive mesh techniques into an air quality model for an ozone case. Zheng et al. (2015) and Zheng et al. (2020) used the anisotropic adaptive mesh technique to accurately represent the air pollutant transport process and chemical reactions. With the rise of grid-independent Galerkin methods and finite volumes (Ford et al. 2004; Nair et al. 2005; Ahmad et al. 2006; Giraldo and Restelli 2008; Giraldo and Warburton 2008; Li et al. 2008; Jablonowski et al. 2009), a number of research studies on dynamic mesh adaptation combined with element-based Galerkin methods have been performed in meteorology applications (Chen et al. 2011; Müller et al. 2013; Yelash et al. 2014; Kopera and Giraldo 2014). Marras et al. (2016) pointed out that element-based Galerkin methods might perform well in next-generation atmospheric and climate models competing with finite difference and spectral transform methods. Savre et al. (2016) first introduced the anisotropic adaptive mesh technique into atmospheric modeling in both horizontal and vertical directions and evaluated it with 2D idealized test cases.

In this study, we develop a new 3D dynamically adaptive atmospheric model (Fluidity-Atmosphere) based on the dynamic framework of Fluidity, a computational fluid dynamic (CFD) model developed by the Applied Modeling and Computation Group (AMCG), Imperial College London (ICL) (Pain et al. 2001, 2005; Piggott et al. 2009). Its accuracy and conservation properties have been validated by a series of idealized simulations using a uniform mesh, and the computational cost has been decreased by mesh adaptivity in rising bubble, density current and interacting warm and cold bubble tests (Pain et al. 2001, 2005; Piggott et al. 2009; Savre et al. 2016; Zheng et al. 2015; 2020). Fluidity-Atmosphere applies dynamically tetrahedral adaptive meshes in 3D space and time so that regions of steep topography, high dynamic activity or specific interest can be modeled with high horizontal and vertical resolutions. The tetrahedral (triangular in 2D) mesh can be adapted in an anisotropic way so that the mesh refinement works on a targeted domain with preferential research requirements (for example, strong convections or local turbulent flows). The adaptive mesh is combined with a range of control volumes and finite element discretization methods to optimally represent flows (e.g., tracers and temperature). With mesh adaptivity, the mass is conserved by a supermesh interpolation strategy (Farrell et al. 2009).

In atmospheric modeling, the computational mesh plays an important role in topographical representation, which is vital for accurately simulating mountain waves and the pressure gradient force. Currently, terrain-following coordinates (Phillips 1957; Gal-Chen and Somerville 1975) are widely used in many NWP models for topographical representation. However, in the vicinity of steep mountains, the nonorthogonality of terrain-following coordinates leads to spurious winds and significant pressure gradient force errors (Sundqvist 1976; Good et al. 2014; Nishikawa and Satoh 2016; Li et al. 2016a). This can be improved, for example, by topographical smoothing with height (Schär et al. 2002; Leuenberger et al. 2010; Klemp 2011; Li et al. 2014) and improvements in the accuracy of schemes for computing the pressure gradient force (Zängl 2012; Li et al. 2012; Weller and Shahrokhi 2014; Li et al. 2016b). Even so, errors are inevitably introduced on ground with unmodified steep terrain in a high-resolution model (Shaw and Weller 2016). An alternative topographical representation is the cut-cell method (Steppeler et al. 2002; Yamazaki and Satomura 2010; Lock et al. 2012; Good et al. 2014). Cut cells and the Galerkin method have in common that the representation of the mountains is achieved by adapting the computational mesh rather than by coordinate transformation. The thin-wall approximation (Steppeler et al. 2002) and grid emerging technique (Yamazaki and Satomura 2010) improved computational efficiency and numerical stability. Steppeler et al. (2006, 2011, 2013, 2019) demonstrated improvements in the prediction of precipitation and potential temperature by the cut-cell method compared with the terrain-following method. Lock et al. (2012) extended a 3D cut-cell approach for steep mountains using piecewise bilinear surfaces. Gallus and Klemp (2000) found that the step-mountain method, representing terrain by a piecewise constant function, can lead to a lack of convergence and artificial flow separation, which cannot even be repaired by a very high vertical resolution. It turned out that representing a mountain by a continuous piecewise linear spline avoids the mentioned difficulties of the step-mountain approach. In Fluidity-Atmosphere, the terrain is embedded within a tetrahedral (triangular in 2D) mesh, similar to the cut-cell method. By specifying the mesh aspect ratio and gradation (smoothness), the flexible mesh adaptivity technique avoids the use of small-size cut cells, thus allowing a large time-step size while maintaining numerical stability.

The performance of Fluidity, including the approximation accuracy, numerical stability, mesh convergence and conservation properties, has been demonstrated by Pain et al. (2001), (2005); Farrell et al. (2009); Piggott et al. (2009); Savre et al. (2016); Li et al. (2018); and Zheng et al. (2015), (2020). One important unanswered question is whether Fluidity-Atmosphere can accurately represent the underlying terrain and simulate mountain waves, which have a dominant effect on atmospheric motions as the horizontal resolution approaches or exceeds $O(10^1)$ *km* (Gallus and Klemp 2000). We conduct a sequence of 2D nonhydrostatic mountain wave tests to evaluate the performance of Fluidity-Atmosphere and then extend them to 3D. In Sect. 2, we introduce the characteristics, governing equations and numerical schemes of Fluidity-Atmosphere. In Sect. 3, we provide the theory of anisotropic adaptive mesh techniques in Fluidity-Atmosphere. In Sect. 4, the performance of adaptive unstructured meshes is tested through a series of 2D and 3D experiments. Sect. 5 evaluates the ability of Fluidity-Atmosphere to accurately represent the underlying terrain. Finally, the conclusions and discussion are presented in Sect. 6.

2. Description of the Fluidity Atmosphere: A Dynamically Adaptive Atmospheric Dynamic Framework

In this work, the dynamic framework of Fluidity-Atmosphere is based on a set of equations within Fluidity (developed by AMCG, ICL), consisting of the continuity equation, nonhydrostatic momentum equation, and energy budget equation. Fluidity has the following features:

- Anisotropic tetrahedral adaptive meshes in 3D space and time such that regions of steep topography, high dynamic activity or specific interest can be modeled with high horizontal and vertical resolutions;
- A range of control volumes and continuous and discontinuous finite element discretization methods;
- Finite element types ($P_N P_M$, where P is a polynomial and N and M are the degrees of the polynomials for velocity and pressure, respectively) designed to optimally represent flows (e.g., tracers and temperature);
- Conservative mesh-to-mesh interpolation;
- Parallel computing.

2.1 Governing Equations

For meteorological applications, the continuity equation, nonhydrostatic momentum equation, energy budget equation, and atmospheric state equations are taken into account as follows:

$$\frac{\partial \rho}{\partial t} = -\nabla \cdot \left(\rho \vec{u} \right) \;, \tag{1}$$

$$\frac{\partial \vec{u}}{\partial t} = -\vec{u} \cdot \nabla \vec{u} - \frac{1}{\rho} \nabla p - \vec{g} - f \vec{k} \times \vec{u} + \vec{D_{\vec{u}}} \;, \tag{2}$$

$$\frac{\partial \Theta}{\partial t} = -\nabla \cdot \left(\vec{u} \Theta \right) - \rho w \frac{\partial \theta_0}{\partial z} + S_\Theta + D_\Theta \;, \tag{3}$$

$$p = p_0 \left(\frac{\rho R_d \theta}{p_0} \right)^{\gamma} \;, \tag{4}$$

where $\nabla = \frac{\partial}{\partial x}\vec{i} + \frac{\partial}{\partial y}\vec{j} + \frac{\partial}{\partial z}\vec{k}$, *t* represents the time, ρ is the dry density, $\vec{u} = (u, v, w)^T = (u_1, u_2, u_3)^T$ is the velocity vector, *p* is the pressure ($p(x,y,z) = p_0(z) + p'(x,y,z)$, where the subscript '0' represents the basic state of the corresponding variable with respect to *z* and *p′* is the perturbation of pressure), $\vec{g}$ is the acceleration of gravity, *f* represents the inertial Coriolis force, $\Theta = \rho\theta - \rho_0\theta_0$ is the perturbation of potential temperature, $\gamma = \frac{c_p}{c_v} = 1.4$ is the ratio of the heat capacities for dry air, $R_d = 281 J \cdot kg^{-1} \cdot K^{-1}$ is the gas constant for dry air, S_Θ refers to the source term of the energy budget equation and $\vec{D_{\vec{u}}}$ and D_Θ are the subgrid turbulent mixing terms, defined as:

$$D_{u_i} = \frac{\partial}{\partial x_j}\left[K_M\left(\frac{\partial u_i}{\partial x_j} + \frac{\partial u_j}{\partial x_i}\right)\right], \tag{5}$$

$$D_\Theta = \frac{\partial}{\partial x_j}\left(K_H \frac{\partial \Theta}{\partial x_j}\right), \tag{6}$$

where x_j represents the *x*-, *y*- and *z*-axes (*j* = 1, 2, 3), K_H is the diffusivity and K_M is the viscosity.

2.2 Discretization of the Governing Equations

Fluidity-Atmosphere employs the mixed continuous/discontinuous Galerkin method for spatial discretization, and a time-stepping λ scheme is adopted for temporal discretization (here, the Crank-Nicolson scheme with $\lambda = 0.5$). For details of the characteristics and numerical schemes in Fluidity-Atmosphere, see AMCG (2014).

Here, we outline the discretization of the equations in Fluidity-Atmosphere. In a finite-element expansion, the velocity components u, v, w and pressure are represented as

$$u_i(X) = \sum_{j=1}^{\aleph} N_{i,j}(X)\, u_{i,j}, \tag{7}$$

$$p(X) = \sum_{j=1}^{\aleph} M_j(X)\, p_j, \tag{8}$$

and the perturbation of potential temperature Θ is:

$$\Theta(X)=\sum_{j=1}^{\aleph}N_{\Theta,j}(X)\Theta_j \ , \tag{9}$$

where $j\in\{1,2,...,\aleph\}$, X is the location of a node; N, M and N_Θ are basis functions for the velocity, pressure and perturbation of potential temperature, respectively; $u_{i,j}, p_j, \Theta_j$ with the subscript 'j' represent the values of the corresponding variables at node *j;* and $\aleph$ is the total number of nodes. Note that in this study, we choose to make the continuity equation test functions the same as the pressure basis functions.

2.2.1 Discretized Momentum Equations

By applying finite elements, the momentum equations are tested with the velocity basis functions $\overrightarrow{N}_i=(N_u,N_v,N_w)$. By applying the λ time-stepping method and taking Eqs. (7) ~ (8) into account, the discrete momentum equations in space can be written in matrix form:

$$\frac{\mathbf{M_U}}{\Delta t}\left(\mathbf{U}^{n+1}-\mathbf{U}^n\right)+\mathbf{A}\left(\mathbf{U}^{n+\lambda_\mathrm{U}}\right)\mathbf{U}^{n+\lambda_\mathrm{U}}+\mathbf{Cp}^{n+1}+\mathbf{B}+\mathbf{Cor}\mathbf{U}^{n+\lambda_\mathrm{U}}=s_\mathbf{U} \ , \tag{10}$$

where $\mathbf{M_U}$ ($M_{\mathbf{U},ij}=\int_\Omega \rho\overrightarrow{N}_i\cdot\overrightarrow{N}_j d\Omega$, and Ω represents the computational domain) denotes the velocity mass matrix; $\mathbf{A}\left(\mathbf{U}^{n+\lambda_\mathrm{U}}\right)$ ($A_{ij}=\int_\Omega \overrightarrow{N}_i\cdot\left(\rho\vec{u}\cdot\nabla\overrightarrow{N}_j\right)d\Omega$) is the advection matrix in the momentum equation; $\mathbf{C}$ ($C_{ij}=\int_\Omega \overrightarrow{N}_i\cdot\nabla M_j d\Omega$) is the pressure gradient matrix; $\mathbf{B}$ ($B_i=\int_\Omega \rho\overrightarrow{N}_i\cdot\vec{g}d\Omega$) is the gravity matrix; $\mathbf{Cor}$ ($Cor_{ij}=\int_\Omega \rho\overrightarrow{N}_i\cdot\left(2\mathbf{\Omega}\times\overrightarrow{N}_j\right)d\Omega$) is the Coriolis force matrix; $\mathbf{U}=\left(\vec{u}_1,\vec{u}_2,...,\vec{u}_\aleph\right)^T$ and $\mathbf{p}=\left(p_1,p_2,...,p_\aleph\right)^T$ are vectors that contain the solutions of the velocity components and pressure over the domain Ω, respectively; $s_\mathbf{U}$ is the source term including the diffusion terms and boundary conditions; and $\mathbf{U}^{n+\lambda_\mathrm{U}}=\lambda_\mathbf{U}\mathbf{U}^{n+1}+\left(1-\lambda_\mathbf{U}\right)\mathbf{U}^n$ (where $0\le\lambda_\mathbf{U}\le 1$).

2.2.2 Discretized Continuity Equation and Pressure Correction

By multiplying the continuity equation with the pressure basis functions M_i and integrating it over the domain, the discrete continuity equations in space can be written in matrix form:

$$\mathbf{M}_\rho \frac{\Delta \boldsymbol{\rho}^n}{\Delta t} + \mathbf{L}\mathbf{U}^n = \mathbf{M}_b q \ , \tag{11}$$

where $\boldsymbol{\rho} = \left(\rho_1, \rho_2, ..., \rho_\aleph\right)^T$; $M_{\rho,ij} = \int_\Omega N_{\rho,i} d\Omega$; $L_{ij} = \int_\Omega \overrightarrow{N}_i \cdot \nabla\left(\rho N_{\rho,j}\right) d\Omega - \int_{\partial\Omega} \rho N_{\rho,j} \overrightarrow{N}_i \cdot \vec{n} d\Omega$; $M_{b,ij} = \int_{\partial\Omega} \rho N_{\rho,j} \overrightarrow{N}_i \cdot \vec{n} d\Omega$ and $q = \vec{u} \cdot \vec{n}$, where $\partial\Omega$ represents the boundary over Ω such that the boundary conditions are applied and the unit vector $\vec{n}$ is assumed to be the outward facing normal vector to the domain Ω. For a given initial pressure or the pressure from the previous time level, an intermediate velocity $\mathbf{u}_*^{n+1}$ can first be solved using Eq. (10). By taking into account Eqs. (10) and (11), the pressure is then corrected using:

$$\mathbf{L}\mathbf{M}_\mathbf{U}^{-1}\mathbf{C}\Delta\mathbf{p}^{n+1} = \frac{\mathbf{L}\mathbf{u}_*^{n+1} - \mathbf{M}_b q}{\Delta t} + \mathbf{M}_\rho \frac{\Delta\boldsymbol{\rho}^{n+1}}{\left(\Delta t\right)^2} \ . \tag{12}$$

The updated pressure is substituted into Eq. (10), and the velocity is recalculated. The combination of determining the momentum and correcting the pressure has to be repeated during the nonlinear iteration procedure until the solutions satisfy both the continuity and momentum equations.

2.2.3 Discretization of the Energy Budget Equations

The discretized form of Eq. (3) at time level n+1 using finite elements and the λ-method is written in a general way as:

$$\mathbf{M}_\mathbf{F} \frac{\mathbf{F}^{n+1} - \mathbf{F}^n}{\Delta t} + \mathbf{A}\left(\mathbf{U}^{n+\lambda_\mathbf{F}}\right)\mathbf{F}^{n+\lambda_\mathbf{F}} = \mathbf{s}_\mathbf{F} \ , \tag{13}$$

where $\mathbf{F} = \left(F_1, F_2, ..., F_\aleph\right)^T$, $F = \Theta$, $M_{\mathbf{F},ij} = \int_{\partial\Omega} N_{F,i} N_{F,j} d\Omega$, $\mathbf{s}_\mathbf{F}$ is the source term, the diffusion terms and the boundary conditions, and $\lambda_\mathbf{F} \in \left[0,1\right]$, where the term $\mathbf{F}^{n+\lambda_\mathbf{F}}$ is given by

$$\mathbf{F}^{n+\lambda_\mathbf{F}} = \lambda_\mathbf{F}\mathbf{F}^{n+1} + \left(1 - \lambda_\mathbf{F}\right)\mathbf{F}^n \ . \tag{14}$$

In Fluidity-Atmosphere, the time-marching algorithm employed uses a nonlinear iteration scheme (AMCG 2014). The time loop is repeated either a fixed number of times or until convergence is achieved. Fig. 1 shows the sequence of steps in the iteration loop.

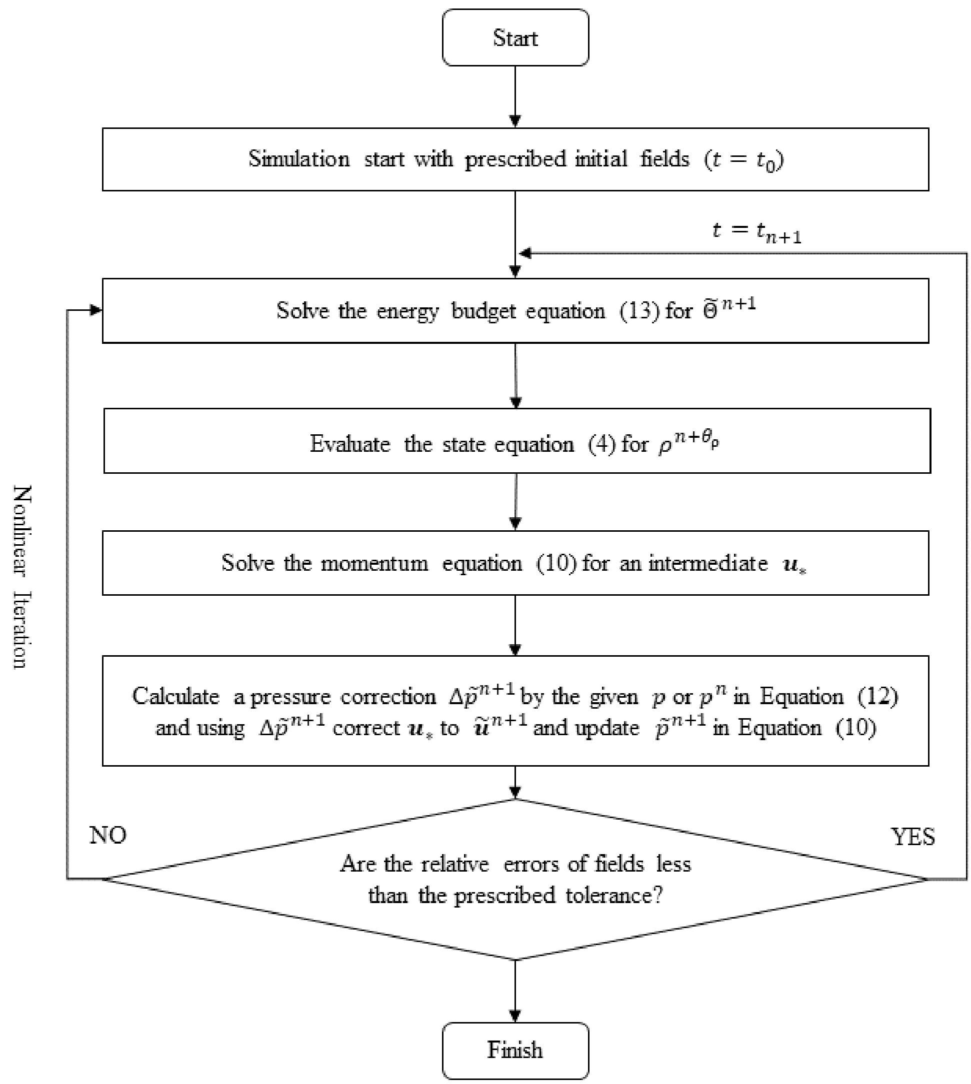

Fig. 1 Time loop of Fluidity-Atmosphere. Note that the variables with wavy lines represent the tentative quantities during the nonlinear iterations for the variables at the next timestep. At the final nonlinear iteration,

$$c^{n+1} = \tilde{c}^{n+1}.$$

3. Introduction of Anisotropic Mesh Adaptive Techniques in Fluidity-Atmosphere

In traditional atmospheric models, adaptive mesh refinement (a locally nested static mesh method) is often used to refine the mesh in local regions. In this work, we introduce an optimization-based adaptive mesh technique (Pain et al. 2001) for atmospheric modeling in both horizontal and vertical directions. Using the optimization-based adaptive technique, the anisotropic unstructured mesh can be dynamically adapted (in time and space) to resolve multiscale flow features as the flow evolves and can capture the details of flows in all three directions (Pain et al. 2001, 2005; Piggott et al. 2009). The mesh adaptivity in Fluidity-Atmosphere is achieved in four steps:

(i) Step 1: Create a one-to-one mapping between the tetrahedral mesh elements $\{e\}$ and the Riemann metric tensor $\bar{\mathbf{M}}$.

(ii) Step 2: Visit all the elements in turn to gauge the mesh quality with the mesh-quality function $\Im$.

(iii) Step 3: Apply the optimization operations in the vicinity of the meshes to improve the mesh quality. The operations include edge collapse, edge splitting, face-to-edge and edge-to-face swapping, edge swapping and node movement.

(iv) Step 4: Interpolate all the information of the variables at the original meshes into the new meshes after mesh adaptivity.

In Step 1, the Riemann metric tensor used to guide the adaptive meshing algorithm can be defined as

$$\bar{\mathbf{M}} = \frac{\gamma}{\varepsilon}\|\mathbf{H}\| , \tag{15}$$

where ε is the required level of error defined by users, γ is an O(1) scalar constant (here, we use $\gamma = 1$) and $\mathbf{H} = \nabla^T \nabla f$ is the Hessian matrix of the state field f that we seek for optimization. The Hessian matrix can be decomposed as

$$\mathbf{H} = \mathbf{V_H} \mathbf{S_H} \mathbf{V}_{\mathbf{H}}^T , \tag{16}$$

where the matrices $\mathbf{V_H}$ and $\mathbf{S_H} = diag\left(\lambda_i^{\mathbf{H}}\right)$ contain the eigenvectors $\mathbf{e}_i$ and eigenvalues $\lambda_i^{\mathbf{H}}$ of the Hessian matrix $\mathbf{H}$, respectively. Then, the operator $\| \cdot \|$ for $\mathbf{H}$ is defined as:

$$\|\mathbf{H}\| = \mathbf{V_H} diag\left(\left|\lambda_i^{\mathbf{H}}\right|\right)\mathbf{V_H}^T \ . \tag{17}$$

To represent small-scale dynamics, a relative error metric formulation is utilized:

$$\bar{\mathbf{M}} = \frac{\gamma\|\mathbf{H}\|}{\max\left(|\sigma|\cdot|f|,|\sigma_{\min}|\right)} \ , \tag{18}$$

where f is the field under consideration, σ is now a relative tolerance, and $\sigma_{\min}$ is the minimum tolerance used to ensure that the denominator never becomes zero. To further control the quality of mesh adaptivity, we can impose some suitable tolerances on the interpolation errors and set restrictions, for example, the minimum and maximum element sizes and aspect ratio, on the mesh. It is also very useful to specify heterogeneous, anisotropic minimum and maximum element sizes for the adaptive mesh.

In Step 2, the mesh quality function is defined as:

$$\Im = \sqrt[p]{\sum_{e=1}^{\aleph}\left(\Im_e\right)^p} = \sqrt[p]{\sum_{e=1}^{\aleph}\left[\frac{1}{2}\sum_{l\in\ell_e}\left(\alpha_l\right)^2+\left(q_e\right)^2\right]^p} \ , \tag{19}$$

where p is the index of the norm used, l is the edge of element e, α_l is a variable used to gauge the deviation of the mesh size compared with a regular tetrahedron, and q_e is a quantity used to evaluate the deviation of the mesh shape compared with a regular tetrahedron with respect to the metric tensor $\bar{\mathbf{M}}$.

In Step 3, the operations of mesh optimization will visit every element in turn and obtain the new computational mesh, then gauge the mesh quality. To determine whether mesh adaptation is executed, we list the criteria for grid refinement:

$$\max_e\left\{\Im_e\right\} - \max_{e'}\left\{\Im'_{e'}\right\} \le -\kappa, \max_e\left\{\Im_e\right\} > \Im_\varepsilon \ , \tag{20}$$

$$\max_e\left\{\Im_e\right\} - \max_{e'}\left\{\Im'_{e'}\right\} \le 0, \frac{1}{\aleph}\max_e\left\{\Im_e\right\} - \frac{1}{\aleph'}\max_{e'}\left\{\Im'_{e'}\right\} \le -\kappa, \max_e\left\{\Im_e\right\} > \Im_\varepsilon \ , \tag{21}$$

where $\Im_e$ and $\Im'_{e'}$ are the original and newly generated mesh-quality functions, $\Im_\varepsilon$ is a certain threshold value (here, we use 0.15), and κ is a controlling parameter. If either Eq. (20) or Eq. (21) is satisfied, mesh adaptation will be implemented. Otherwise, the mesh returns to the previous status.

In Step 4, a mass-conserving interpolation approach, the Galerkin projection (Farrell et al. 2009; Savre et al. 2016), is utilized to interpolate solutions from the previous mesh to the newly generated adaptive mesh, which is implemented by a supermeshing algorithm. For the details of the grid adaptivity measurements, we refer to AMCG (2014).

4. Idealized Mountain Wave Test Cases

In this section, the performance of Fluidity-Atmosphere using anisotropic adaptive unstructured meshes is evaluated with three test scenarios:

(i) nonhydrostatic flow in a stable stratified atmosphere around a 2D bell-shaped mountain (Lock et al. 2012);

(ii) sensitivity analysis of the mountain wave results with respect to different adaptive mesh sizes in the horizontal and vertical directions;

(iii) a sequence of experiments simulating nonhydrostatic flow over the 3D steep bell-shaped hill specified in Lock et al. (2012);

Here, the dynamically adaptive mesh technique ensures computational effort in resolving the dynamic flow process over a wide range of spatial scales.

4.1 2D Adaptive Nonhydrostatic Mountain Wave

In this test, we use the benchmark 2D test of Lock et al. (2012) for flow over a bell-shaped mountain with steady boundary conditions to form a stable upward-propagating mountain wave in a stratified atmosphere.

The computational domain is 60 *km* wide in the horizontal direction and 16 *km* deep in the vertical direction, with a simulation time of 50000 *s*. The timestep is set to 5.0 *s,* and mesh adaptation is performed every 10 timesteps. The anisotropic gradation and maximum aspect ratio are restricted to 2 and 10, respectively. Before the actual simulation starts, the mesh is adapted twice to capture the basic information of the initial fields. The resolution of the adaptive meshes varies from 0.2 *km* to 2 *km* with respect to the solution of the state variables (the velocity vector here), while the absolute interpolation error is set to 0.1 in the horizontal direction and 0.02 in the vertical direction. For comparison purposes, the control run is conducted in a fixed mesh with horizontal and vertical resolutions of $dx = dz = 0.2\ km$ (Fig. 4).

For spatial discretization, continuous Galerkin (CG) and control volume (CV) methods are applied. The basis functions *N*, *M* and N_Θ used to approximate the velocity, pressure and perturbation of the potential temperature are first order. For the CV method, the face value is obtained by first-order upwind discretization or alternatively by using finite element interpolation (hereafter referred to as CV1 and CV2, respectively, AMCG, 2014). For temporal discretization, we utilize the semi-implicit Crank-Nicolson scheme with $\lambda = 0.5$.

The underlying 2D bell-shaped mountain is defined as:

$$h(x) = \frac{h_0}{1 + \frac{x^2}{a^2}}, \tag{22}$$

where $h_0 = 400m$ is the maximum height of the mountain and the half-width of the mountain is $a = 1000m$. We use a constant Brunt-Väisälä frequency of $N = 0.01s^{-1}$ to define the stratified background, and the bottom potential temperature is $\theta_0 = 293.15K$. The initial velocity of the flow is $\vec{u} = (10,0)^T\ m/s$. We apply no-flux boundary conditions along the bottom surface. Open lateral boundary conditions are used at the inflow and outflow boundaries. Since $\frac{Na}{u} = 1$, this test belongs to the nonhydrostatic range based on the analysis in Gallus and Klemp (2000).

To prevent the oscillation of the waves reflected at the top and the lateral boundaries, an absorbing layer is added on the top of the model, and strong diffusion is included at the lateral boundaries. In the outermost $z_s = 6km$ at the top of the model, a damping coefficient α is set after the prediction at the *n*-th time step:

$$\alpha = \begin{cases} -\alpha_{\max}\left[1 - \cos\left(\frac{\pi}{2}\frac{z - z_s}{z_{top} - z_s}\right)\right], \text{for } z_s < z < z_{top}, \\ 0, \qquad\qquad\qquad\qquad\qquad \text{otherwise.} \end{cases}, \tag{23}$$

where $z_{top} = 16km$ such that the damped model solutions ϕ (including u, v, w, Θ) at the *n*-th time step become:

$$\phi_n = \phi_n^0 + \alpha\left(\phi_n^0 - \phi_0\right) \ , \tag{24}$$

where ϕ_0 is the initial state of the variable ϕ and ϕ_n^0 is the variable after the *n*-th time step without damping. Here, $\alpha_{\max} = 1$.

For stability, we define two continuous diffusions K_L and K_V, where K_L is the diffusion for the lateral boundaries:

$$K_L = \begin{cases} K_L^{\max}, & \text{for } x_{out} < x < x_b, \\ K_L^{\max} \dfrac{x - x_{in}}{x_{out} - x_{in}}, & \text{for } x_{in} < x < x_{out}, \\ 0, & \text{otherwise,} \end{cases} \tag{25}$$

and K_V is the diffusion in the vertical direction:

$$K_V = \begin{cases} K_V^{\max}, & \text{for } z_{bot} < z < z_a, \\ K_V^{\max} \dfrac{z_b - z}{z_b - z_a} + K_V^{\min}, & \text{for } z_a < z < z_b, \\ 0, & \text{otherwise,} \end{cases} \tag{26}$$

where $K_H^{\max} = 50000 m^2/s$; x_{in} and x_{out} are the innermost and outermost positions for using diffusion, in which the diffusion ranges linearly from 0 to $K_H^{\max}$; and x_b is the position of the boundaries. Here, $\left[x_{in}, x_{out}, x_b\right] = \left[10, 6, 0\right] km$ at the inflow boundary and $\left[50, 54, 60\right] km$ at the outflow boundary. $K_V^{\max} = 500 m^2/s$ and $K_V^{\min} = 100 m^2/s$; $z_a = 3km$ and $z_b = 4km$ are the starting and ending boundaries for the linear range of K_V in the vertical direction from $K_V^{\min}$ to $K_V^{\max}$, and $z_{bot} = 0$. Thus, the diffusion is defined as:

$$K = K_L + K_V \ . \tag{27}$$

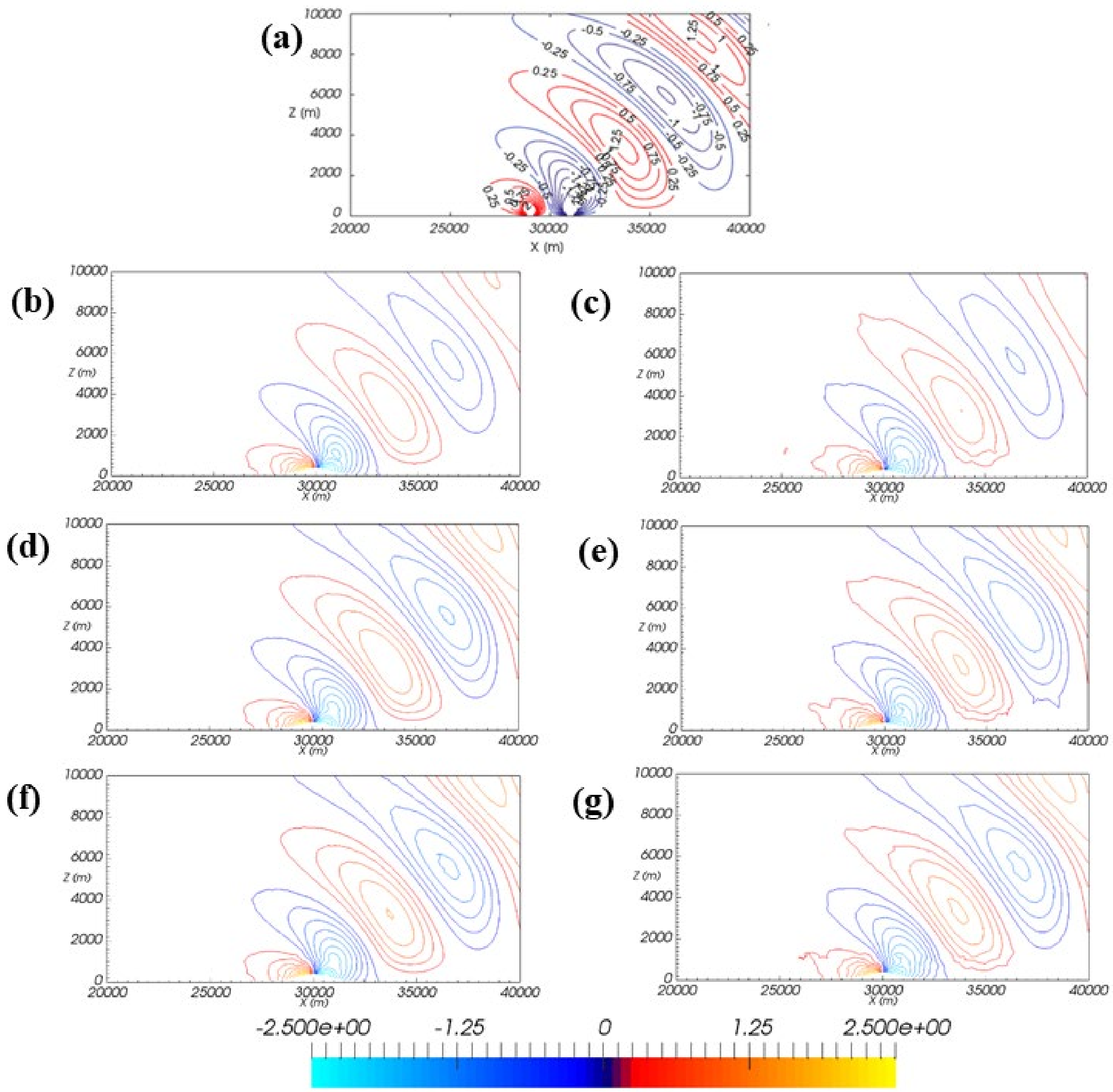

Fig. 2 Vertical velocity solution for the mountain wave simulation over a 2D bell-shaped terrain with a contour interval of 0.25 *m/s*. (**a**): The analytic solution reproduced from Gallus and Klemp (2000); (**b**) and (**c**): the solutions of the CV1 method; (**d**) and (**e**): the solutions of the CV2 method; (**f**) and (**g**): the solutions of the CG method. (**b**), (**d**) and (**f**) are for a fixed mesh, while (**c**), (**e**) and (**g**) are for an adaptive mesh.

Fig. 2 illustrates the contours of the vertical velocity until a steady-state velocity is achieved by (a) linear theory (Gallus and Klemp 2000); (b), (e) CV1; (c), (f) CV2; and (d), (g) CG. The analytic solution is obtained using Eq. (4) with linear theory for a flow past the step mountain of Gallus and Klemp (2000). The left and right columns are the results for fixed and adaptive meshes, respectively. All the flow patterns using Fluidity-Atmosphere show good agreement with the analytic solution, and the contours of the vertical velocity are stacked vertically above the terrain. A comparison between the results for the fixed mesh and the adaptive mesh reveals that the adaptive mesh is able to simulate mountain waves with a similar quality as the fixed mesh. The deviations from the analytic solution with respect to the magnitude of the vertical velocity among CV1, CV2 and CG exhibit a declining trend. The CV1 method (Fig. 2b and 2c) shows a smaller velocity farther from the peak of the mountain because the first-order upwind scheme is less accurate. The pattern and center position of the wave in CV2 (Fig. 2d and 2e) and CG (Fig. 2f and 2g) are comparable to those of the analytic solution (Fig. 2a). Moreover, the results for the fixed mesh exhibit smooth vertical velocity contours, while a few numerical artifacts can be detected at the periphery of the contours (e.g., the outermost contour) for all the adaptive-mesh cases. This may be seen as a small error arising from adaptivity.

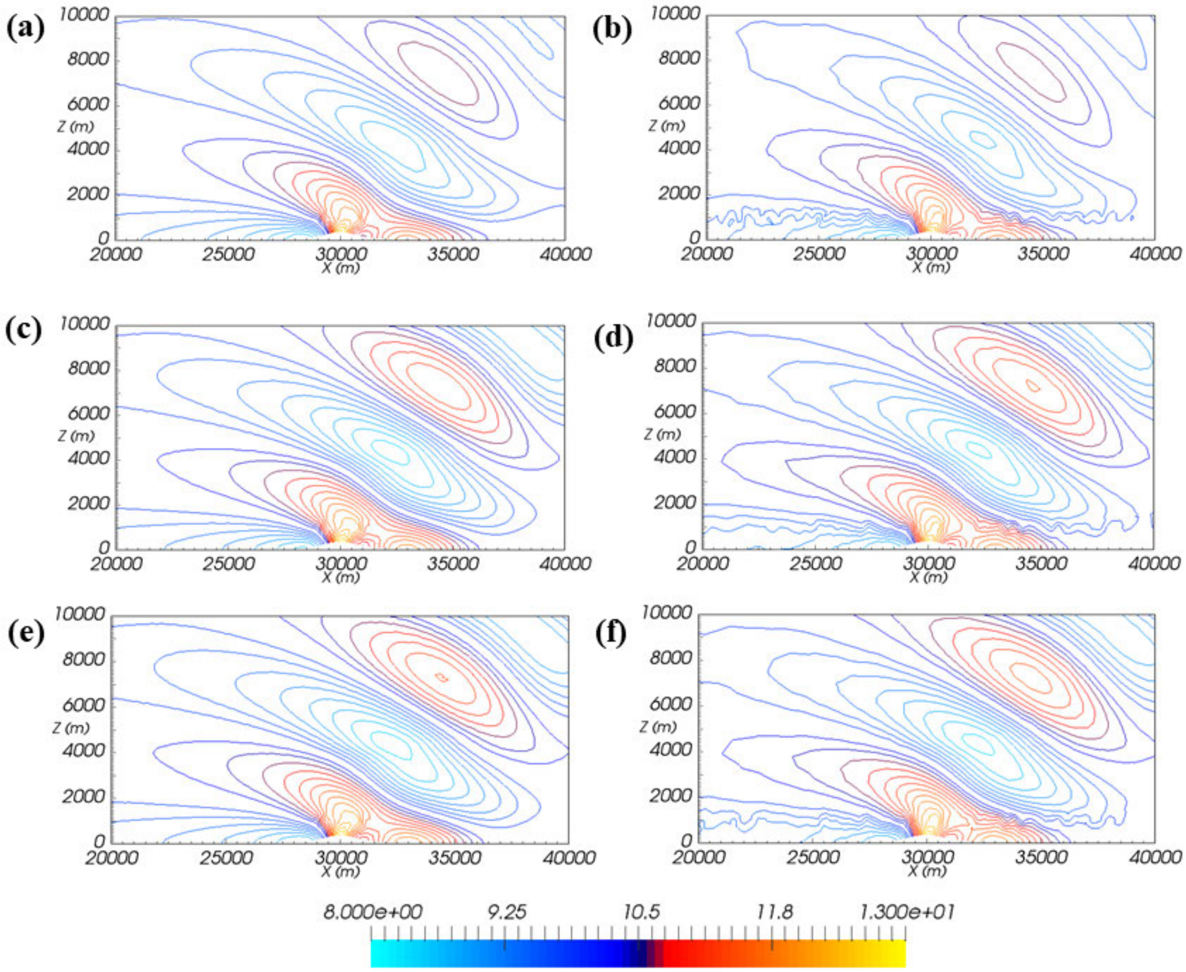

Fig. 3 Horizontal velocity solution and the corresponding adaptive mesh for the mountain wave simulation over a 2D bell-shaped terrain with a contour interval of 0.2 *m/s*. The left column contains all the results for the fixed mesh, while the right column shows those of the adaptive mesh. (**a**) and (**b**): The solutions of the CV1 method; (**c**) and (**d**): the solutions of the CV2 method; (**e**) and (**f**): the solutions of the CG method.

Fig. 3 shows the horizontal velocity contours. Small artificial noise in the vicinity of the mountain at a height of almost 1 *km* occurs with the adaptive mesh cases. The spurious oscillation on the entire bottom boundary is incorrectly captured by the adaptive meshes and is thus artificially amplified in the vicinity of the mountain. This can be observed correspondingly for the adaptive mesh snapshot in Fig. 4.

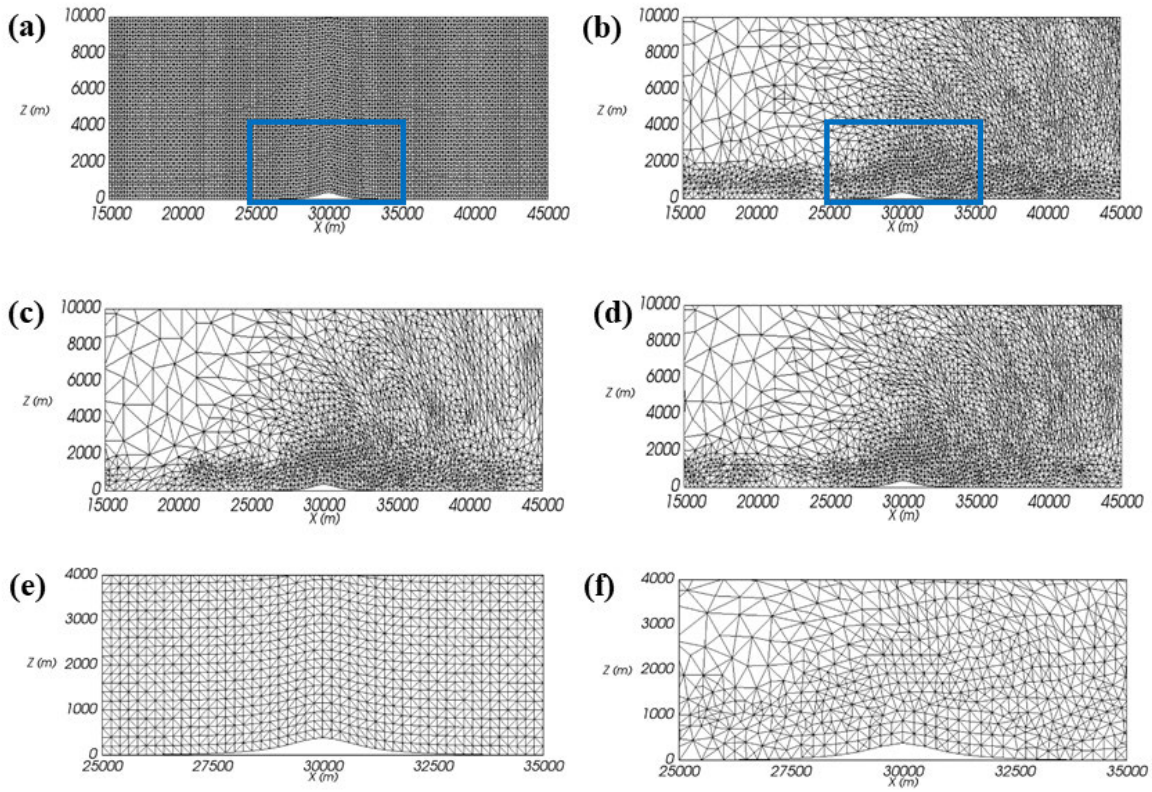

Fig. 4 Computational meshes for the mountain wave simulation over a 2D bell-shaped terrain. (**a**): Terrain-following triangular fixed meshes with $dx = dz = 200$ m; (**b**), (**c**) and (**d**): anisotropic adaptive meshes with the CG, CV1 and CV2 methods. The maximum and minimum lengths are 2000 m and 200 m. (**e**) and (**f**) show the magnified views of (**a**) and (**b**) marked by the blue rectangular areas.

Compared with the CG results, the CV1 and CV2 methods possess an intrinsic viscosity (diffusion). Although an increase in $K_V^{\max}$ makes the numerical noise disappear, it is accompanied by a reduction in the magnitude of the velocity. Therefore, in order to eliminate the noise around the peak of the mountain and maintain the magnitude of the velocity, partial node locking at the bottom boundary will be conducted in Sect. 5.

Table 1 The number of cells and points used for the fixed mesh and the adaptive mesh in Sect. 4.1.

Number of Cells/Points	Spatial Discretization	Fixed Mesh	Adaptive Mesh	
			Start (t = 0 s)	Steady (t = 50000 s)
Cells	CV1	48000	1447	6064
	CV2	48000	1447	8914
	CG	48000	1447	9596
Points	CV1	24381	644	3132
	CV2	24381	644	4560
	CG	24381	644	4901

The relationship between the mesh refinement and computational costs for the fixed mesh and the adaptive mesh was investigated. The meshes for the simulation are shown in Fig. 4, and the number of cells and points and the corresponding ratios of the adaptive mesh and the fixed mesh are provided in Tabs. 1 ~ 2. The fixed mesh is composed of triangular meshes based on terrain-following quadrilaterals that are cut into two triangles by one diagonal line. The numbers of cells and points in the fixed mesh are constant values of 48000 and 24381, respectively. In contrast, the adaptive mesh changes every 10th timestep, so we present the numbers at the start time and at the time when the steady solution is reached. We note that the mesh is adapted with respect to the velocity such that the entire domain is filled with coarse meshes before the activation of the mountain wave. Then, at the steady state, the wave continuously propagates downstream and upward from the peak of the mountain, leading to a high-resolution dense mesh aggregated on the entire leeward side of the mountain. Due to the decay of the velocity magnitude with height, the mesh becomes coarser than the mesh in the vicinity of the mountain, as shown in Figs. 4b ~ 4d. The mesh adaptivity therefore reduces the number of cells and points to 6064 ~ 9596 and 3132 ~ 4901. The corresponding ratio of the adaptive mesh and the fixed mesh becomes 12.7% for CV1, 18.6% for CV2 and 20% for CG. The ratio of runtimes between the adaptive mesh and the fixed mesh is proportional to the ratio of the number of nodes and cells. Therefore, to achieve the desired accuracy, the adaptive mesh requires fewer computational nodes and a shorter runtime through the whole domain, thus improving the computational efficiency compared to the fixed mesh. Moreover, for the adaptive mesh, the difference in accuracy in the vertical velocity among CV1, CV2 and CG can be reflected by the difference in the number of cells and points in these test cases. In other words, the greater the number of cells and points, the higher the accuracy achieved.

Table 2 Three ratios of the adaptive mesh and the fixed mesh at t = 50000 s from the six mountain wave tests presented in Sect. 4.1.

Ratio	CV1	CV2	CG
Number of Cells	12.63%	18.57%	19.99%
Number of Points	12.85%	18.70%	20.10%
Runtime	13.11%	18.28%	23.56%

4.2 2D Adaptive Nonhydrostatic Mountain Wave with Different Resolutions and the Relation to the Cut Cells

Our study now focuses on the resolution dependence of mountain wave modeling using adaptive mesh techniques. In this study, the simulations of the mountain wave are set up as in Sect. 4.1 except for the setting of the adaptive meshes. Since the performance of the CG method is superior to that of the CV methods, CG will be utilized in the following tests. To evaluate the impact of the horizontal (vertical) resolution, we keep the minimum vertical (horizontal) mesh size at 200 m, while the minimum horizontal (vertical) mesh size is 1600, 800, 400, 200, 100 and 50 m.

The results with variations in the horizontal mesh size are shown in Fig. 5. These results (the accuracy and location of the wave contours) agree well with the analytic solution except for those for the coarse mesh scheme. According to the increase in the horizontal mesh resolution, the amplitudes of the vertical velocity are increased somewhat positively at the peak of the mountain, and the contour of the vertical velocity becomes smooth, although there is slight noise on the bottom boundary. However, when the mesh size is less than 200 m, the effect of increasing the horizontal resolution is not obvious in terms of smoothness, and the continuity of the solution is different from the results in Gallus and Klemp (2000) (Figs. 5e and 5f). This is because Fluidity-Atmosphere enables a piecewise continuous mountain representation to achieve convergence, especially for high horizontal resolution.

In detail, the scheme in Fluidity-Atmosphere is very similar to the cut-cell formulation for the representation of mountains, which is achieved by mesh adaptation instead of coordinate transformation. In fact, for the fixed mesh study, the scheme in Fluidity-Atmosphere is a cut-cell formulation (using an unstructured mesh). For the unstructured adaptive mesh used here, the problem of the appearance of very small cells, typical for cut cells, is not present. As a mountain is represented here by piecewise linear spline results, we are free from the problems pointed out by Gallus and Klemp (2000) for mountain representations by piecewise constant splines. This result is in full agreement with Steppeler et al. (2002), who concluded that the problems for Gallus and Klemp (2000) disappear when the bottom boundary is changed to a piecewise linear mountain. Furthermore, cut cells allow the presence of steep mountains, which will be addressed in Sect. 4.3.

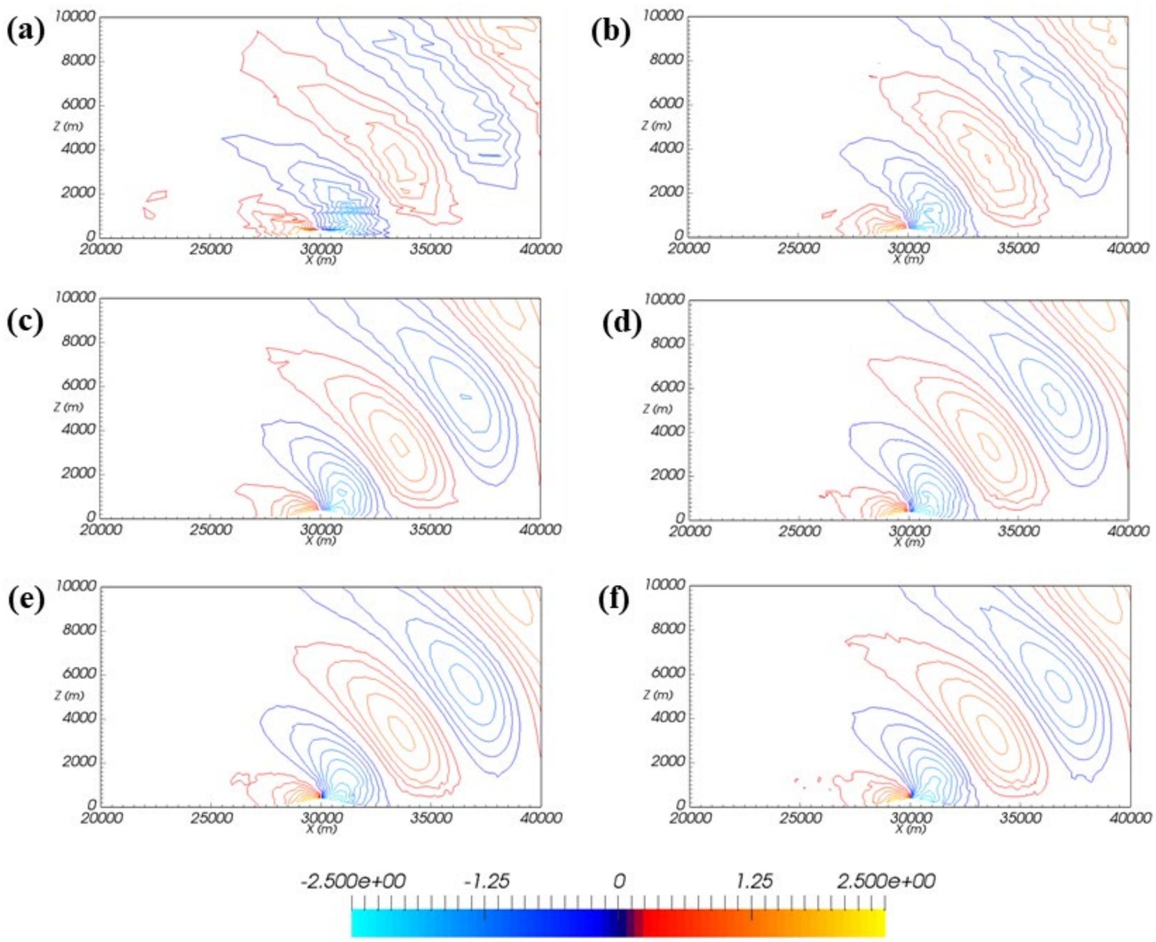

Fig. 5 Vertical velocity solution of the mountain wave simulation over a 2D bell-shaped terrain with different horizontal mesh sizes. The maximum mesh size in both the horizontal and vertical directions is 2000 *m,* and the minimum vertical mesh size is 200 *m*. The minimum horizontal mesh sizes are (**a**) 1600 *m*, (**b**) 800 *m*, (**c**) 400 *m*, (**d**) 200 *m*, (**e**) 100 *m* and (**f**) 50 *m*. The contour interval is 0.25 *m/s*.

With the increase in vertical resolution shown in Fig. 6, the vertical velocity contour is near the analytic solution. Similar to the result in Fig. 5a, the coarse-resolution simulation result (dz = 1600 m in Fig. 6a) exhibits very strong vertical oscillations, especially for the area over the peak of the mountain. The error can be reduced by increasing the vertical resolution (Figs. 6b~6d). When further increasing the vertical resolution to dz = 50 m from 200 m, both the smoothness and the magnitude of the contours are always preserved (Figs. 6d ~ 6f). Combined with the results in Figs. 5d ~ 5f, dx = dz = 200 m should be a wise choice for Fluidity-Atmosphere in the 2D mountain-wave simulation. We note that the maximum height of the mountain is 400 m, so the increase of the vertical resolution has a strong impact on the representation of the terrain when dz < 400 m. Because it is different from the step-mountain coordinate, the adaptive mesh in Fluidity-Atmosphere makes the underlying terrain smoother. Therefore, judging from the contours of the velocity contour, Fluidity-Atmosphere maintains its characteristics at dz = 200 m.

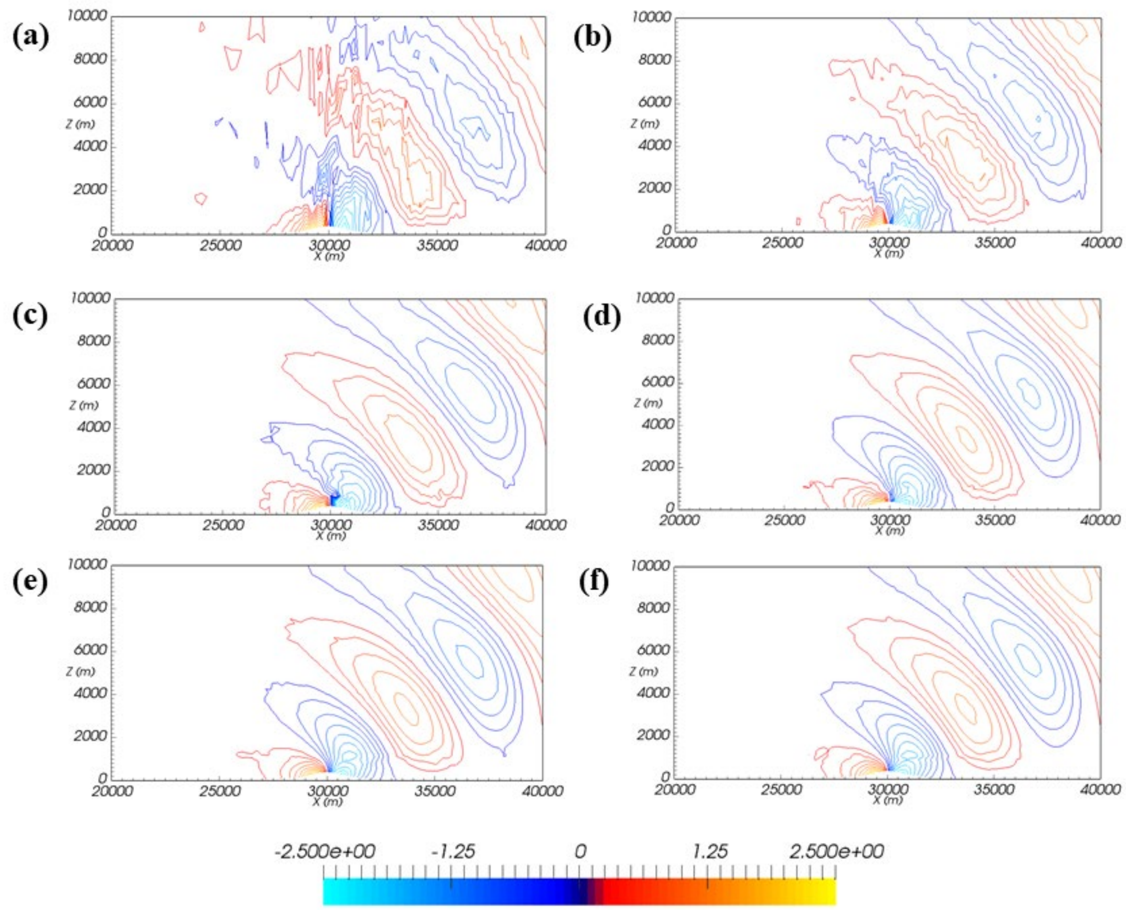

Fig. 6 Vertical velocity solution of the mountain wave simulation over a 2D bell-shaped terrain with different vertical mesh sizes. The maximum mesh size in both the horizontal and vertical directions is 2000 *m,* and the minimum horizontal mesh size is 200 *m*. The minimum vertical mesh sizes are (**a**) 1600 *m*, (**b**) 800 *m*, (**c**) 400 *m*, (**d**) 200 *m*, (**e**) 100 *m* and (**f**) 50 *m*. The contour interval is 0.25 *m/s*.

4.3 3D Adaptive Nonhydrostatic Mountain Wave

To demonstrate the accuracy and stability of 3D Fluidity-Atmosphere, we extend the benchmark test of Lock et al. (2012) to 3D. The computational domain is 60 *km* wide in both horizontal directions and 16 *km* deep in the vertical direction with a simulation time of 15000 *s*. The resolution of the adaptive meshes varies from 0.125 *km* to 10 *km*. Mesh adaptation is performed every 5 timesteps. All other parameters related to mesh adaptivity are kept the same as those in Sect. 4.1.

The underlying 3D bell-shaped mountain is defined as:

$$h(x,y)=\frac{h_0}{\left(1+\frac{x^2+y^2}{a^2}\right)^{\frac{3}{2}}} \ , \tag{22}$$

where $h_0 = 400m$ is the maximum height of the mountain and the half-width of the mountain is $a = 1000m$. The stratified background state is defined by $N = 0.01s^{-1}$, and the potential temperature at the bottom surface is $\theta_0 = 293.15K$. The initial velocity of the flow is $\vec{u} = (10,0,0)^T \ m/s$. To prevent the oscillation of the waves reflected at the top and lateral boundaries, the treatments for the top and lateral boundaries of the model used in Sect. 4.1 are also applied here.

The stable and smooth solution is shown in Fig. 7. In Fig. 7a, the mountain wave propagates upward from the peak of the mountain, and its strength decays with height. In the horizontal *x-y* slice at *z* = 2 *km* (Fig. 7b), the contour of the vertical velocity is very smooth and symmetric. The same symmetric distinguishing pattern can be seen in the vertical cross-section at *x* = 32 *km* downstream of the mountain (Fig. 7c), although slight noise appears at approximately *z* = 1 *km*. In the horizontal slice at *z* = 800 *m* (Fig. 7d), a little noise appears in the outermost layer of the contour.

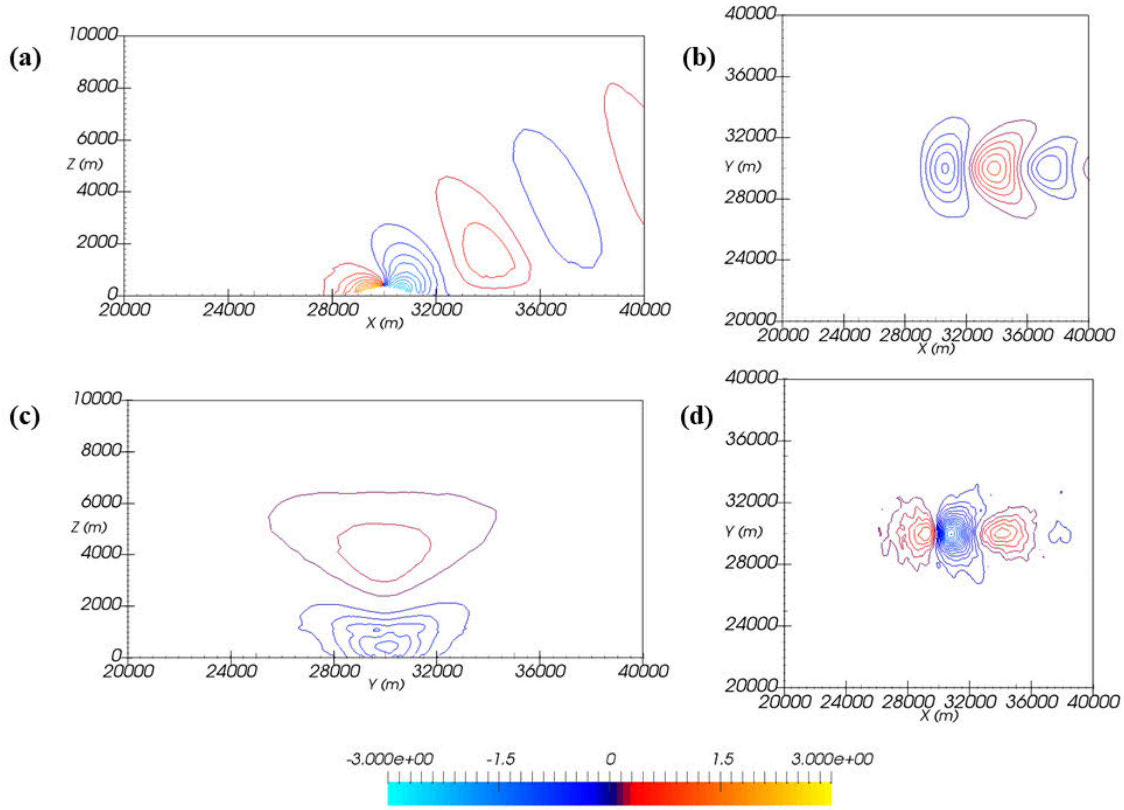

Fig. 7 Contours of the vertical velocity for the mountain wave simulation over a 3D bell-shaped terrain. (**a**) Vertical cross-section through the center of the mountain at y = 30 *km* with a contour interval of 0.25 *m/s*; (**c**) vertical cross-section at x = 32 *km*, which is 2 *km* downstream of the peak of the mountain and has a contour interval of 0.1 *m/s*; (**b**) and (**d**) horizontal cross-sections at heights z = 2000 *m* and z = 800 *m* with a contour interval of 0.1 *m/s*, respectively.

Both results are comparable to the results of Fig. 7 in Lock et al. (2012, hereafter referred to as Lock Fig. 7), although there is a little noise along the bottom due to the use of the unstructured adaptive mesh. The center positions and amplitudes of the waves shown at the *x-z* and *y-z* slices are in good agreement in the vicinity of the mountain. When x > 38 *km,* the height of the third contour of the positive vertical velocity in Fig. 7a is slightly higher than that in Lock Fig. 7a. Furthermore, the magnitudes of the extreme centers at the peak of the mountain at the horizontal cross-sections (z = 2000 *m* and z = 800 *m*) are consistent with those of Lock Figs. 7b and 7d. Only the maximum value of the negative extreme center downstream of the mountains is slightly smaller than that of Lock Figs. 7b and 7d, 0.1 *m/s*.

Fig. 8 shows the 3D adaptive mesh in three cross-sections, which is used to capture the mountain wave features. Fig. 8c is the 3D perspective of Fig. 8a. We note that the mesh is denser in the area with higher velocity gradients and relatively sparser in the remainder of the domain.

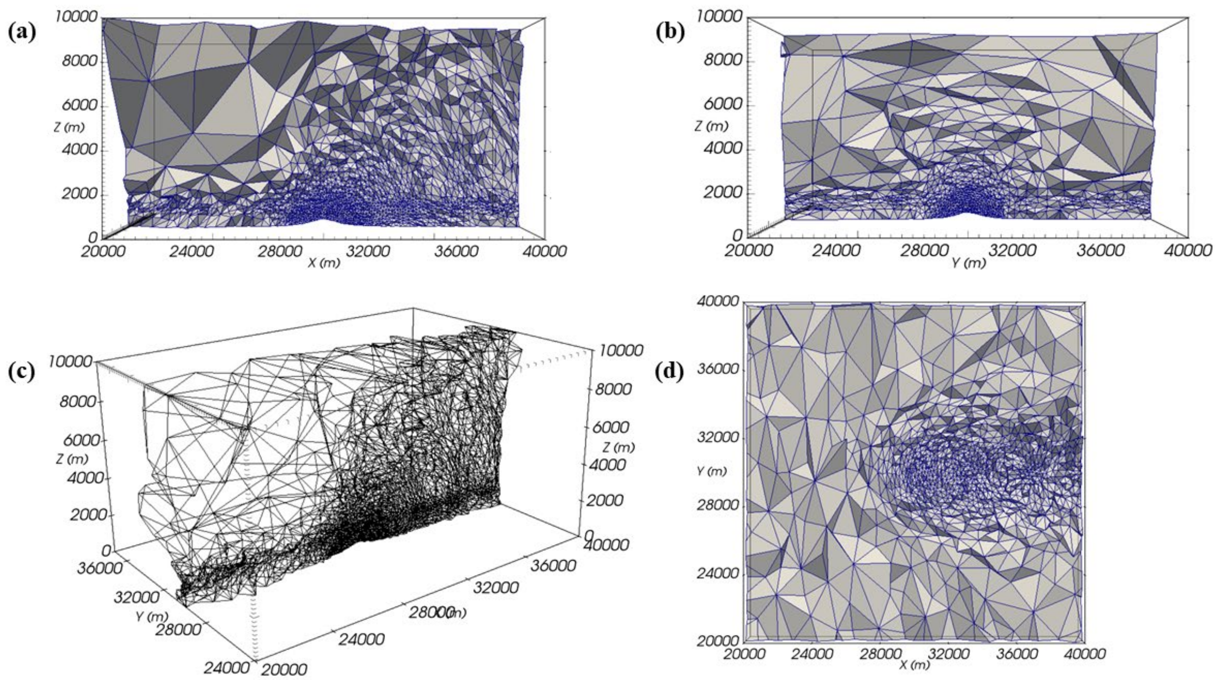

Fig. 8 Anisotropic adaptive meshes for the vertical field for the mountain wave simulation over a 3D bell-shaped terrain. (**a**) Vertical crinkle cross-section through the center of the mountain at y = 30 km; (**b**) vertical crinkle cross-section at x = 32 km, which is 2 km downstream of the peak of the mountain; (**c**) 3D perspective of (**a**) and (**d**), horizontal cross-section at height z = 2000 m.

To further evaluate the stability and accuracy of Fluidity-Atmosphere for a steep mountain in a high-resolution simulation, we conducted another test case with $h_0 = 2000m$ and $a = 1000m$, while the other parameters remained the same.

The vertical velocity of the steep mountain with $h_0 = 2000m$ and $a = 1000m$ at $t = 10000s$ is shown in Fig. 9. For this case, the coefficient representing the nonlinearity of the flow is $\frac{Nh_0}{u} = 2 > 1$, which means that the flow is strongly nonlinear (Lilly and Klemp 1979; Ikawa 1988; Gallus and Klemp 2000; Zängl et al. 2015). In this situation, although the linear theory of mountain waves is invalid and the mountain waves break, the vertical velocity from the steep mountain has the same pattern as that shown in Fig. 7 with $h_0 = 400m$. Naturally, the greater height of the mountain produces a stronger perturbation of the vertical velocity. Stacked velocity contours and a decay in height at the vertical cross-section at y = 30 *km* are observed. The properties of smoothness and symmetry are also seen at the vertical cross-section at x = 32 *km* and at the horizontal cross-sections at heights z = 2000 and 4000 *m*. A little noise at the outermost area of the contours is still detected at z = 800 *m*. Due to the use of adaptive meshes similar to cut-cells, semi-implicit temporal discretization and the CG method, the result remains relatively stable in the case of such a steep mountain.

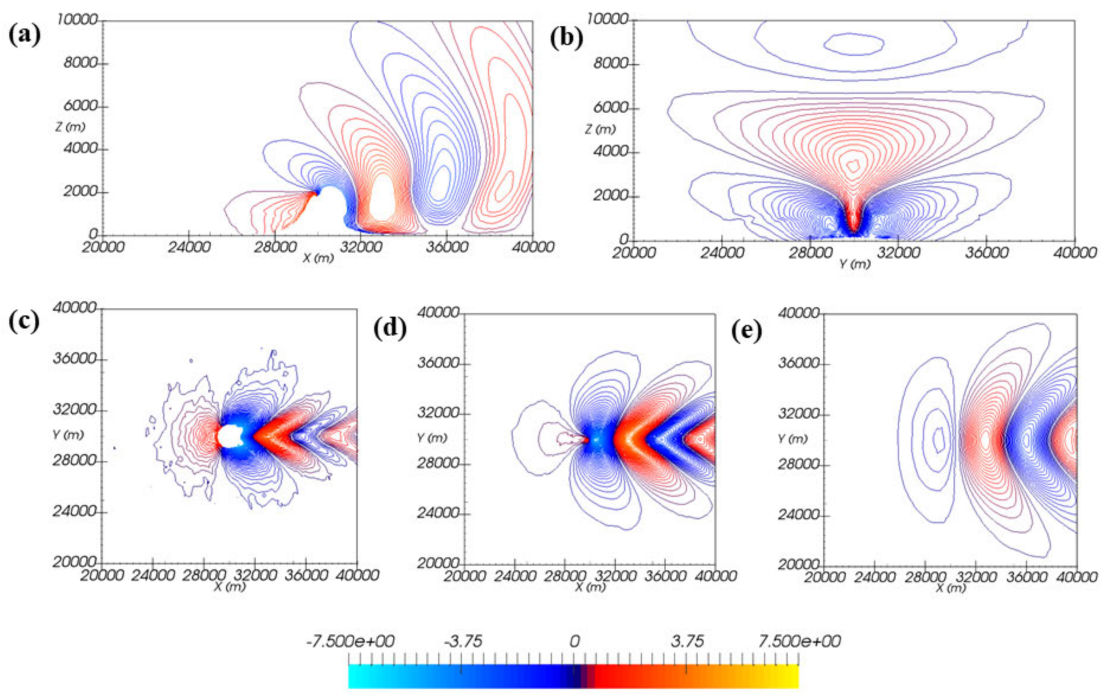

Fig. 9 Contour of the vertical velocity solution for the mountain wave simulation over a 3D bell-shaped terrain. (**a**) Vertical cross-section through the center of the mountain at y = 30 *km*; (**b**) vertical cross-section at x = 32 *km*, which is 2 *km* downstream of the peak of the mountain; (**c**), (**d**) and (**e**) horizontal cross-sections at heights z = 800, 2000, 4000 *m*, respectively. The contour intervals are 0.25 *m/s* for (a) and 0.1 *m/s* for all the others. The model solutions are represented at t = 10000 *s*.

5. Accuracy of the Orographic Representation

The sufficient condition for accurately representing the underlying mountain in terrain-following coordinates is $\Delta h < \Delta z$, where Δh and Δz are the deviation of the orographic height between two neighboring horizontal grid points and the vertical resolution, respectively (Ikawa 1988; Steppeler et al. 2006). However, the ability to obtain an accurate orographic representation would be hindered if the slope of the mountain became very steep or the resolution of the NWP models increased. This is because the vertical resolution would be very coarse to satisfy the condition $\Delta h < \Delta z$ with a large Δh for high and steep mountains. During some numerical procedures, high and steep mountains may even lead to linear instability (Ikawa 1988). This error and potential instability can be removed by the use of cut-cell grids or cut-cell structures. Cut-cell structures are horizontally aligned, which means that the grid lines of the cells are cut into the mountain (for a review of cut-cell methods, see Steppeler et al. 2002 or Yamazaki and Satomura 2010). Due to the resemblance between the adaptive mesh of Fluidity-Atmosphere and the cut-cell grid, it is interesting to see whether Fluidity-Atmosphere can be used to accurately represent the terrain, thus reducing the spurious wind. In this section, based on the test case in Sect. 4.1, two simulations are conducted by (i) giving a perturbation of the potential temperature in the entire computational domain and (ii) using the treatment of node locking in the vicinity of the mountain while keeping the other parameters identical to those in Sect. 4.1.

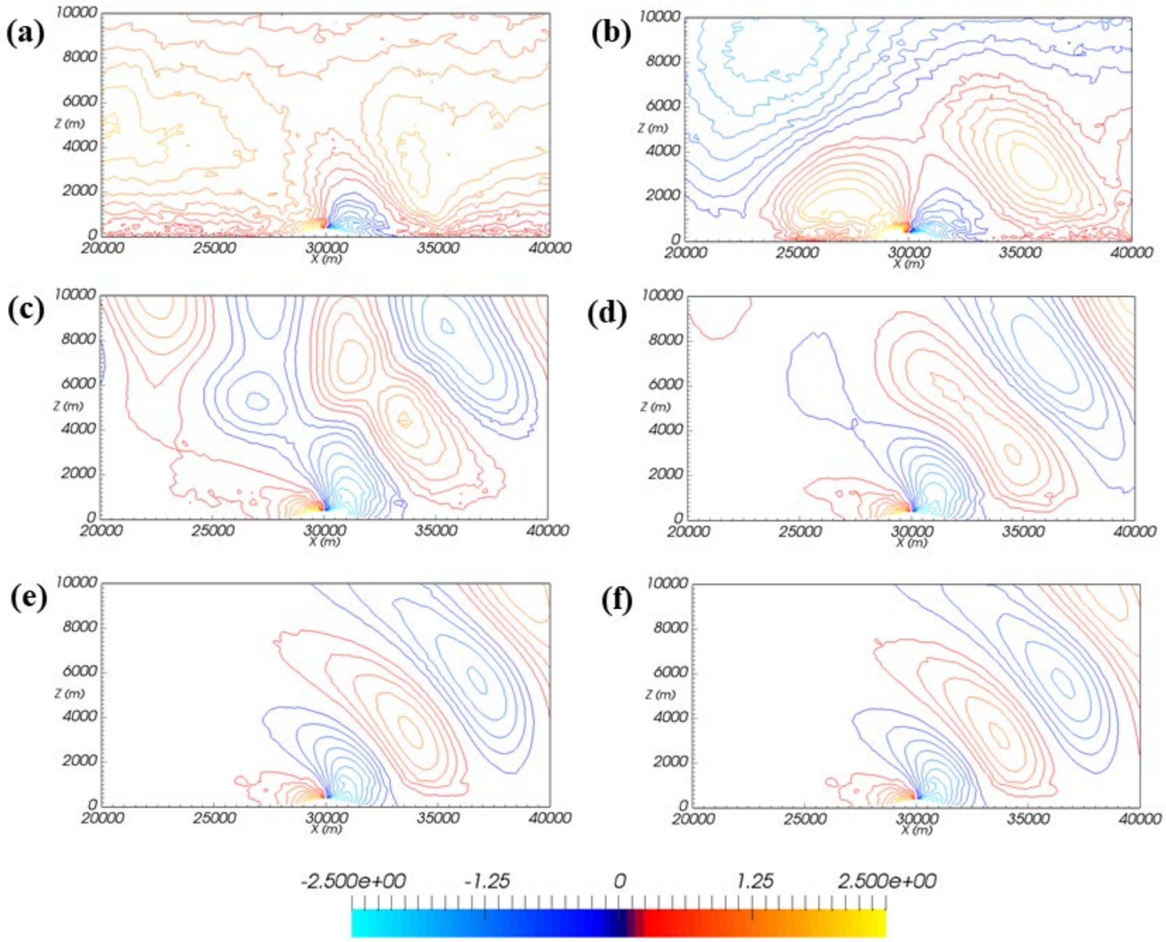

Fig. 10 Contour of the vertical velocity solution for the mountain wave simulation over a 2D bell-shaped terrain with a constant perturbation of the potential temperature $\Delta\theta = 5K$. The contour interval is 0.25 *m/s*. (**a**) ~ (**f**) show the results at t = 500, 1000, 3000, 6000, 12000 and t = 20000 *s*.

First, we introduce an extra potential perturbation of a constant $\Delta\theta = 5K$ over the entire domain (see Saito et al. 1998), while the setup of the test case in Sect. 4.1 is repeated. In this case, the ratio $\frac{\Delta h}{\Delta z}$ is less than 1.0. The time integrations continue until a steady-state velocity is achieved without any physical parameterization. Figs. 10 and 11 show the vertical perturbations and the adaptive mesh, respectively, at t = 500, 1000, 3000, 6000, 12000 and 20000 *s* with the CG method and a damping operation. At the beginning of the simulation, the potential temperature perturbation stimulates the formation of the vertical velocity in the whole computational domain (Fig. 10a), leading to the aggregation of adaptive meshes in the entire domain (Fig. 11a). With a sustained horizontal velocity (constant), the impact of the potential temperature perturbation gradually becomes evanescent (Fig. 10b). At t = 3000 s, the contours of the mountain wave become visible (Fig. 10c). The induced perturbations of the vertical velocity distribute throughout the domain in such a way that the adaptive mesh remains dense (Fig. 11c). With the disappearance of the noise at the inflow and top boundaries, the mesh is adapted to be coarse upstream of the mountain (Figs. 11d ~ 11f). Although an orographic representation error appears at the beginning, this spurious wind is reduced with the CG method and the adaptive mesh of the cut-cell form in Fluidity-Atmosphere (Figs. 10d ~ f). In the vicinity of the terrain, the larger Δz (compared to Δh) inhibits the development of instability, and the adaptive grid makes the orography smooth with the use of high-resolution meshes. Compared with Fig. 2g, both results are in good agreement, and the features of the mountain waves are reproduced, including the stacked vertical velocity contours and the decay of the strength with the height. Therefore, Fluidity-Atmosphere can accurately represent the underlying terrain and eliminate the spurious winds induced by the perturbation of the potential temperature. The errors in the terrain-following coordinates are reduced because the adaptive mesh forms a smoothly varying mountain in Fluidity-Atmosphere.

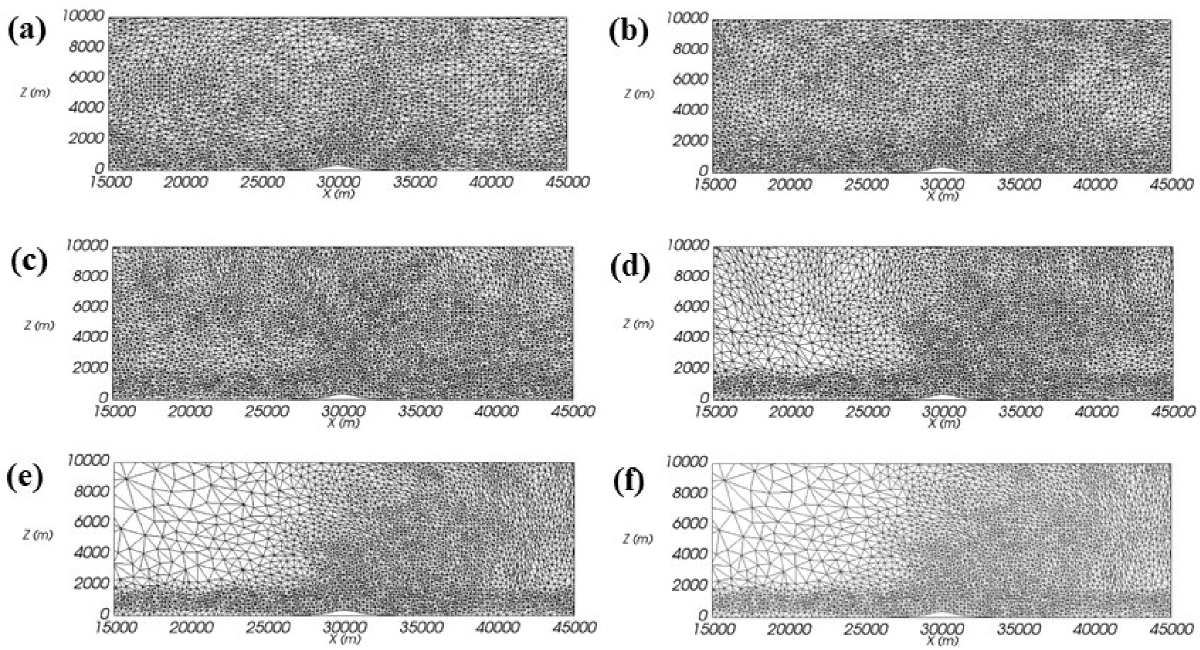

Fig. 11 The evolution of the adaptive mesh for the mountain wave simulation over a bell-shaped terrain of height 400 *m* and half-width 1000 *m* with a constant perturbation of potential temperature $\Delta\theta = 5K$. (a) ~ (f) show the results at *t* = 500, 1000, 3000, 6000, 12000 and *t* = 20000 *s*.

Second, to reduce the numerical noise near the bottom in the adaptive mesh (Figs. 2c, 2e and 2g), the mesh along the bottom boundary is locked. Furthermore, to achieve the stability condition $\Delta h < \Delta z$, we lock the terrain-following mesh under the height of 2000 *m* as a fixed coarse mesh with *dx* = *dz* = 200 *m*. All the other parameters are kept the same as those in Sect. 4.1. Because the maximum derivative of the mountain height $\frac{\partial h}{\partial x} < 0.3$ leads to $\Delta h = \frac{\partial h}{\partial x} dx < 60$, the condition is satisfied ($\Delta h < 60 < \Delta z$). The adaptive mesh and the contour of the velocity components at *t* = 50000 *s* are shown in Fig. 12.

The noise in the vicinity of the mountain is eliminated by the node-locking treatments for both the vertical and horizontal components of the velocity using the adaptive mesh. A comparison between the fixed mesh (Figs. 2f and 3e) and the adaptive mesh with node locking (Fig. 12) reveals that the adaptive mesh is feasible for orographic representation and that the mountain wave simulation achieves the same precision with a lower computational cost than that of the fixed mesh.

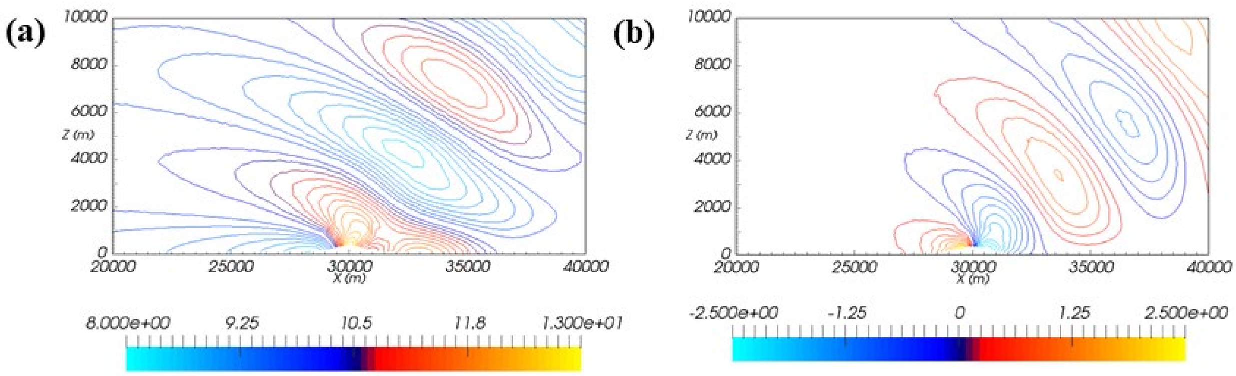

Fig. 12 Contour of the velocity solution and the corresponding mesh for the mountain wave simulation over a 2D bell-shaped terrain with node locking on the bottom boundary. (**a**) The horizontal velocity contour with a contour interval of 0.2 *m/s* and (**b**) the vertical velocity contour with a contour interval of 0.25 *m/s* of Fluidity-Atmosphere with the CG method.

6. Conclusions

In this study, we investigate the ability of the Fluidity-Atmosphere dynamic framework to simulate 3D mountain waves. In general, the 3D anisotropic adaptive and highly irregular mesh of Fluidity-Atmosphere performs well in simulations of mountain waves. The anisotropic adaptive mesh provides an alternative to capture mountain wave fronts propagating upward and downstream. The scheme used in Fluidity-Atmosphere can be seen as an adaptive and irregular mesh version of the cut-cell approach with a piecewise linear mountain representation.

For instance, Fluidity-Atmosphere is able to generate smooth, symmetric and stable mountain waves for the flow past a bell-shaped mountain. Compared to the performance on smooth mountains (Fig. 7), Fluidity-Atmosphere also performs well by almost eliminating mesh-scale oscillations on steep mountains (Fig. 9). As an alternative to the cut-cell grid, the adaptive mesh coupled with the Galerkin method can eliminate the noise in the entire domain introduced by the strong perturbation of the potential temperature. The characteristics of mountain waves and the underlying terrain are accurately represented through automatic aggregation of the adaptive meshes. The sensitivity analysis of the mesh resolution demonstrates that the variation in the horizontal and vertical resolutions has a strong impact on the smoothness of the results and maintains convergence even at high resolutions. Currently, in order to eliminate the noise at the bottom boundary for the simulation of mountain waves, we settled for the second-best solution, which is to lock the nodes at the bottom boundary. How to choose the mesh refinement criteria to distinguish noise and prognostic variables with comparable magnitudes should be taken into consideration in the future work.

Acknowledgments

No author reported any potential conflicts of interest. This work is jointly supported by the National Natural Science Foundation of China (Grant No. 41905093), the China Scholarship Council (No. 201904910136) and Special Research Assistant Project of Chinese Academy of Sciences. Drs. Fang and Wu acknowledge the support of UK EPSRC grant: Managing Air for Green Inner Cities (MAGIC: Grant No. EP/N010221/1).

Data availability statement

The datasets generated during the current study are available from the corresponding author on reasonable request.

References

Ahmad N, Bacon D, Hall M, Sarma A (2006) Application of the multidimensional positive definite advection transport algorithm (MPDATA) to environmental modelling on adaptive unstructured grids. Int J Numer Methods Fluids 50: 1247–1268.

AMCG (2014) Fluidity manual. Applied Modelling and Computation Group, Imperial College London, URL http://fluidityproject.github.io/support.html.

Bacon DP, Ahmad NN, Boybeyi Z, Dunn TJ, Hall MS, Lee PCS, Sarma RA, Turner MD (1999) A dynamically adapting weather and dispersion model: The operational multiscale environment model with grid adaptivity (OMEGA). Mon Wea Rev. 128: 2044–2076, doi:10.1175/1520-0493(2000)128<2044:ADAWAD>2.0.CO;2.

Chen C, Xiao F, Li X (2011) An adaptive multimoment global model on a cubed sphere. Mon Wea Rev 139: 523–548.

Doms G, Baldauf M (2018) A description of the nonhydrostatic regional model COSMO-Model. Part I: Dynamics and Numerics. Consortium for small-scale modelling (COSMO-Model 5.5) Techical Report DWD Germany, http://www.cosmo-model.org/content/model/documentation/core/default htm.

Farrell P, Piggott M, Pain CC, Gorman G, Wilson C (2009) Conservative interpolation between unstructured meshes via supermesh construction. Comput Method Appl M 198: 2632–2642.

Ford R, Pain CC, Piggot M, Goddard A, Oliveria C, Umpleby A (2004) A nonhydrostatic finite-element model for threee-dimensional stratified oceanic flows. Part I: Model formulation. Mon Wea Rev 132: 2816–2831.

Gal-Chen T, Somerville R (1975) On the use of a coordinate transformation for the solution of the Navier-Stokes equations. J Comput Phys 17: 209–228.

Gallus WA, Klemp JB (2000) Behavior of flow over step orography. Mon Wea Rev 128: 1153–1164.

Garcia-Menendez F, Odman M (2011) Adaptive grid use in air quality modelling. Atmosphere 2(3): 484–509.

Giraldo F, Restelli M (2008) A study of spectral element and discontinuous galerkin methods for the Navier-Stokes equations in nonhydrostatic mesoscale atmospheric modelling: Equation sets and test cases. J Comput Phys 227, 3849–3877.

Giraldo F, Warburton T (2008) A high-order triangular discontinuous galerkin oceanic shallow water model. Int. J. Numer Methods Fluids 56: 899–925.

Good B, Gadian A, Lock S, Ross A (2014) Performance of the cut-cell method of representing orography in idealized simulations. Atmos Sci Lett 15: 44–49.

Ikawa M (1988) Comparison of some schemes for nonhydrostatic models with orography. J Meteor Soc Japan 66: 753–776.

Iselin JP (2002) Dynamic grid adaptation using the mpdata scheme. Mon Wea Rev 130: 1026–1039, doi:10.1175/1520-0493(2002)130<1026:DGAUTM>2.0.CO;2.

Jablonowski C, Oehmke R, Stout Q (2009) Block-structured adaptive meshes and reduced grids for atmospheric general circulation models. Philos Trans R Soc A 367: 4497–4522.

Janjic Z (2003) A nonhydrostatic model based on a new approach. Meterol Atmos Phys 82: 271–285.

Karamchandani P, Vijayaraghavan K, Yarwood G (2011) Subgrid scale plume modelling. Atmosphere 2(4): 389–406.

Klemp JB (2011) A terrain-following coordinate with smoothed coordinate surfaces. Mon Wea Rev 139: 2163–2169.

Kopera M, Giraldo F (2014) Analysis of adaptive mesh refinement for imex discontinuous galerkin solutions of the compressible euler equations with application to atmospheric simulations. J Comput Phys 275: 92–117.

Kühnlein C (2011) Solution-adaptive moving mesh solver for geophysical flows. Ludwig-Maximilians-Universität München 1–14, https://core.ac.uk/download/pdf/11032937.pdf.

Leuenberger D, Koller O, Fuhrer O, Schär C (2010) A generalization of the sleve vertical coordinate. Mon Wea Rev 138: 3683–3689.

Li J, Li Y, Wang B (2016a) Characteristics of pressure gradient errors in a terrain-following coordinate. Atmos Oceanic Sci Lett 9 (3): 211–218.

Li J, Li Y, Wang B (2016b) Pressure gradient errors in an alternative approach of implementing sigma coordinate: geometric analyses and idealized experiments. Atmos Oceanic Sci Lett 9 (4): 270–276.

Li J, Zheng J, Zhu J, Fang F, Pain CC, Steppeler J, Navon MI, Xiao H (2018) Performance of adaptive unstructured mesh modelling in idealized advection cases over steep terrains. Atmosphere 9: 444.

Li X, Chen D, Peng X, Takahashi K, Xiao F (2008) A multimoment finite volume shallow water model on Yin-Yang overset spherical grid. Mon Wea Rev 136: 3066–3086.

Li Y, Wang B, Wang D (2012) Anewapproach to implement sigma coordinate in a numerical model. Commun Computat Phys 12: 1033–1050.

Li Y, Wang B, Wang D, Li J, Dong L (2014) An orthogonal terrain-following coordinate and its preliminary tests using 2-D idealized advection experiments. Geosci Model Dev 7: 1767–1778.

Lilly D, Klemp JB (1979) The effect of terrain shape on non-linear hydrostatic mountain waves. J Fluid Mech 95: 241–261.

Lock SJ, Bitzer HW, Coals A, Gadian A, Mobbs S (2012) Demonstration of a cut-cell representation of 3D orography for studies of atmospheric flows over very steep hills. Mon Wea Rev 140: 411–424.

Marras S, Kelly JF, Moragues M, Müller A, Kopera MA, Vázquez M, Giraldo FX, Houzeaux G, Jorba O (2016) A review of element-based galerkin methods for numerical weather prediction: Finite element, spectral elements, and discontinuous galerkin. Arch Computat Methods Eng 23: 673–722, doi:10.1007/s11831-015-9152-1.

McClatchey R, Fenn R, Selby J, Volz F, Garing J (1972) Optical properties of the atmosphere. Air Force Cambridge Research Lab Bedford MA 411: 3–9.

Müller A, Behrens J, Giraldo F, Wirth V (2013) Comparison between adaptive and uniform discontinuous Galerkin simulations in dry 2D bubble experiments. J Comput Phys 235: 371– 393.

Nair R, Thomas S, Loft R (2005) A discontinuous Galerkin global shallow water model. Mon Wea Rev 133: 876–888.

Nishikawa Y, Satoh M (2016) A conserved topographical representation scheme using a thin-wall approximation in z-coordinate. SOLA 12: 232–236, doi:10.2151/sola.2016-046.

Odman M, Khan M (2002) Adaptive grid air qualitymodel: Application to an ozone episode. Proceedings of the 12th Joint Conference on the Applications of Air Pollution Meteorology with the Air and Waste Management Association Norfolk VA USA.

Odman M, Khan M, Srivastava R, McRae D (2004) Initial application of the adaptive grid air quality model, in book: Air Pollution Modeling and Its Application XV. Springer 319–328.

Pain CC, Piggott MD, Goddard AJH, Fang F, Gorman GJ, Marshall DP, EatonMD, Power PW, Oliveira CRE (2005) Three dimensional unstructured mesh ocean modelling. Ocean Model 10: 5–33.

Pain CC, Umpleby A, Oliveira CD, Goddard A (2001) Tetrahedral mesh optimisation and adaptivity for steady-state and transient finite element calculations. Comput Method Appl M 190: 3771–3796.

Phillips NA (1957) A coordinate system having some special advantages for numerical forecasting. J Meteor 14: 184–185.

Pielke RA, Cotton WR, Walko RL, Tremback CJ, Lyons WA, Grasso LD, Nicholls ME, Moran MD, Wesley DA, Lee TJ, Copeland JH (1992) A compressible meteorological modeling system–RAMS. Meterol Atmos Phys 49: 69–91.

Piggott M, Farrell P, Wilson C, Gorman G, Pain CC (2009) Anisotropic mesh adaptivity for multi-scale ocean modelling. Philos T R Soc A 367: 4591–4611.

Saito K, Doms G, Schättler U, Steppeler J (1998) 3D mountain waves by the LOKAL model of DWD and the MRI mesoscale nonhydrostatic model. Pap Meteor Geophys 49: 7–19.

Savre J, Percival J, Herzog M, Pain CC (2016) Two-dimensioanl evaluation of ATHAM-FLUIDITY, a nonhydrostatic atmospheric model using mixed continuous/discontinuous finite elements and anisotropic grid optimization. Mon Wea Rev 144: 4349–4372, doi: 10.1175/MWR-D-15-0398.1.

Schär C, Leuenberger D, Fuhrer O, Lüthi D, Girard C (2002) A new terrain-following vertical coordinate formulation for atmospheric prediction models. Mon Wea Rev 130: 2459–2480.

Shaw J, Weller H (2016) Comparison of terrain-following and cut-cell grids using a nonhydrostatic model. Mon Wea Rev 144: 2085–2099.

Skamarock W, Klemp JB (1993) Adaptive grid refinement for two-dimensional and three-dimensional nonhydrostatic atmospheric flow. Mon Wea Rev 121: 788–804.

Skamarock W, Klemp JB, Dudhia J, GIll D, Baker D, WangW, Powers J (2007) A description of the advanced research WRF Version 2. Tech Rep NCAR TN STR, 468.

Skamarock W, Oliger J, Street R (1989) Adaptive grid refinement for numerical weather prediction. J Comput Phys 80: 27–60.

St-Cyr A, Jablonowski C, Dennis J, Henry H, Thomas S (2008) A comparison of two shallow water models with noncomforming adaptive grids. Mon Wea Rev 136(6): 1898–1922.

Steppeler J, Li J, Navon IM, Fang F, Xiao Z (2019) Medium range forecasts using cut-cells: a sensitivity study. Meteorol Atmos Phys doi:10.1007/s00703-019-00681-w.

Steppeler J, Minotte HBM, Bonaventura L (2002) Nonhydrostatic atmospheric modeling using a z-coordinate representation. Mon Wea Rev 130: 2143–2149.

Steppeler J, Park S, Dobler A (2011) A 5-day hindcast experiment using a cut-cell z-coordinate model. Atmos Sci Lett 12: 340–344.

Steppeler J, Park S, Dobler A (2013) Forecasts covering one month using a cut-cell model. Geosci Model Dev 6: 875–882.

Steppeler J, Bitzer HW, Janjic Z, Schättler U, Prohl P, Gjertsen U, Torrisi L, Parfinievicz J, Avgoustoglou E, Damrath U (2006) Prediction of clouds and rain using a z-coordinate nonhydrostatic model. Mon Wea Rev 134: 3625–3643.

Sundqvist H (1976) On vertical interpolation and truncation in connexion with use of sigma system models. Atmosphere 14: 37–52.

Weller H, Browne P, Budd C, Cullen M (2016) Mesh adaptation on the sphere using optimal transport and the numerical solution of a Monge–Ampère type equation. J Comput Phys 308: 102–123, doi:10.1016/j.jcp.2015.12.018.

Weller H, Shahrokhi A (2014) Curl-free pressure gradients over orography in a solution of the fully compressible euler equations with implicit treatment of acoustic and gravity waves. Mon Wea Rev 142: 4439–4457.

Yamazaki H, Satomura T (2010) Nonhydrostatic atmospheric modeling using a combined Cartesian grid. Mon Wea Rev 132: 3932–3945.

Yang X, Hu J, Chen D, Zhang H, Shen X, Chen J, Ji L (2008) Verification of grapes unified global and reginal numerical weather prediction model dynamic core. Chin Sci Bull 53: 3458–3464.

Yelash L, Müller A, Lukacova-Medvidova M, Giraldo F, Wirth V (2014)Adaptive discontinuous evolution Galerkin method for dry atmospheric flow. J Comput Phys 268: 106–133.

Zängl G (2012) Extending the numerical stability limit of terrain-following coordinate models over steep slopes. Mon Wea Rev 140: 3722–3722.

Zängl G, Reinert D, Ripodas P, Baldauf M (2015) The ICON (icosahedral non-hydrostatic) modelling framework of DWD and MPI-M: Description of the non-hydrostatic dynamical core. Quart J Roy Meteor Soc 141: 563–579.

Zheng J, Fang F, Wang Z, Zhu J, Li J, Li J, Xiao H, Pain CC (2020) A new anisotropic adaptivemesh photochemical model for ozone formation in power plant plumes. Atmos Environ 229: 117431.

Zheng J, Zhu J, Wang Z, Fang F, Pain CC, Xiang J (2015) Towards a new multiscale air quality transport model using the fully unstructured anisotropic adaptive mesh technology of Fluidity (version 4.1.9). Geosci Model Dev 8: 3421–3440.